PHYSICAL REVIEW B **90**, 174424 (2014)

Intra- and interparticle magnetism of cobalt-doped iron-oxide nanoparticles encapsulated in a synthetic ferritin cage

E. Skoropata,[1] R. D. Desautels,[1] E. Falvo,[2] P. Ceci,[2] O. Kasyutich,[3] J. W. Freeland,[4] and J. van Lierop[1]
[1] *Department of Physics and Astronomy, University of Manitoba, Winnipeg, Manitoba, Canada R3T 2N2*
[2] *CNR, Institute of Biology, Molecular Medicine and Nanobiotechnology, Rome, Italy*
[3] *Engineering Faculty, University of Bristol, Bristol, United Kingdom*
[4] *Advanced Photon Source, Argonne National Laboratory, Argonne, Illinois 60439, USA*

(Received 3 July 2014; revised manuscript received 28 September 2014; published 18 November 2014)

We present an in-depth examination of the composition and magnetism of cobalt (Co^{2+})-doped iron-oxide nanoparticles encapsulated in *Pyrococcus furiosus* ferritin shells. We show that the Co^{2+} dopant ions were incorporated into the γ-Fe_2O_3/Fe_3O_4 core, with small paramagnetic-like clusters likely residing on the surface of the nanoparticle that were observed for all cobalt-doped samples. In addition, element-specific characterization using Mössbauer spectroscopy and polarized x-ray absorption indicated that Co^{2+} was incorporated exclusively into the octahedral B sites of the spinel-oxide nanoparticle. Comparable superparamagnetic blocking temperatures, coercivities, and effective anisotropies were obtained for 7%, 10%, and 12% cobalt-doped nanoparticles, and were only slightly reduced for 3% cobalt, indicating a strong effect of cobalt incorporation, with a lesser effect of cobalt content. Due to the regular particle size and separation that result from the use of the ferritin cage, a comparison of the effects of interparticle interactions on the disordered assembly of nanoparticles was also obtained that indicated significantly different behaviors between undoped and cobalt-doped nanoparticles.

DOI: 10.1103/PhysRevB.90.174424 PACS number(s): 76.80.+y, 75.75.Fk, 75.75.Jn, 78.20.Ls

I. INTRODUCTION

Substantial interest has developed surrounding ferritin-based nanoparticle systems due to the numerous intrinsic advantages for the development of "idealized" nanoparticle systems. That is, the ferritin cage prevents agglomeration and interparticle exchange interactions and results in predictable interparticle separation due to the well-defined cage thickness. In addition, the ferritin cage constrains the particle growth, leading to monodisperse nanoparticles. *Pyrococcus furiosus* ferritin (PfFt), in particular, has several unique advantages, such as enabling a "gentle" reactive environment that can lead to the formation of materials that are difficult to obtain at the nanoscale using conventional free solution environments [1], having a high thermal stability [2], and producing well-crystallized samples [1] due to the relatively few internal nucleation sites for mineralization; qualities which lead to good tunability and a high-quality nanoparticle that is ideal for the examination of nanoparticle magnetism. Importantly, ferritin-based nanoparticles are also particularly well suited as building blocks for macroscopic self-assembly that provides an avenue for the study of dipolar-driven magnetism [1,3–5].

While reactions in ferritins involve only Fe ions naturally, a variety of particles (oxide, metallic and semiconductor [1,6,7]) have been remineralized with various ferritins. By incorporating Co^{2+} ions into the spinel Fe-oxide cores, the intrinsic anisotropy of the nanoparticle may be enhanced substantially. However, due to the differences between confined reactions in the ferritin vessel (which contain specific nucleation and catalytic sites and are a highly charged environment) and the fundamental difference in the nature of the surface environments in comparison with surfactant-coated nanoparticles produced freely in solution, a detailed examination of the composition and magnetism of the ferritin-based nanoparticle is necessary. An understanding of the intrinsic properties of the individual nanoparticles is also an essential prerequisite to developing an understanding of the macroscopically assembled systems [8].

In this work, we examine the relationship between the composition, structure, and resulting magnetism of 0%–12% (atomic) cobalt (Co^{2+})-doped iron-oxide nanoparticles. These nanoparticles were prepared using the artificial ferritin cage PfFt, and all the ionic impurities and external aggregates were stripped off. The well-crystallized and uniformly separated nanoparticle systems provided ideal platforms for examining the intrinsic magnetism and interparticle interactions (behavior masked typically by secondary effects such as a large size distributions and particle agglomeration). Using overall, atomic, and elemental magnetism characterization techniques, we find that no change in the Co^{2+} coordination environment occurs among the series; Co^{2+} was incorporated exclusively into the octahedral sites of the Fe-oxide-based core that, in turn, affected the orbital moment of cobalt. The incorporation of Co^{2+} into the Fe-oxide core increased substantially the anisotropy of the nanoparticle, although not systematically with cobalt content. A clear comparison revealing the nature of the interparticle interactions was enabled as the ferritin shell provided a consistent interparticle separation between systems and prevented exchange interactions from altering the local, atomic magnetism among nanoparticles (i.e., from metal-to-metal contact between nanoparticles). We found that the interactions had a significant effect on the dynamical freezing (e.g., time-dependent magnetism) of the cobalt-doped nanoparticles' magnetizations, indicating longer-range correlations among nanoparticles with Co doping. Simultaneously, similar long-range effective fields (e.g., dipolar in nature) due to essentially identical nanoparticle spacial arrangements between samples were measured.

II. EXPERIMENT

A. Sample preparation

Fe-oxide, and cobalt-doped Fe-oxide nanoparticles in the ferritin were mineralized in the synthetic ferritin *Pyrococcus furiosus* (PfFt) as described in Ref. [9]. Following mineralization, aggregates on the exterior of the nanoparticles were removed using centrifugation, filtration using 0.2-μm filters, and size-exclusion chromatography as described in Ref. [10]. In addition, to be sure that the filled nanoparticles were extracted from the unfilled protein shells, we used the high gradient magnetic separation method described in Ref. [11]. Briefly, PfFt nanoparticles were passed through a column containing steel powder to which we applied a magnetic field of ~0.6 T using a permanent magnet. The nanoparticle solutions containing fixed amounts of metals were dried on a SpeedVac SC110 rotary evaporator at 4 °C (Thermo Fisher Scientific, Waltham, MA).

B. Experimental techniques

X-ray diffraction (XRD) patterns were collected under ambient conditions using dried nanoparticle samples on a zero-background quartz slide. XRD patterns were collected using a Brüker D8 Discover using Cu K_α radiation. The lattice parameters, crystallite size (due to Scherrer broadening), and octahedral site occupancy were determined from Rietveld refinements of the XRD patterns using FULLPROF [12].

Transmission Mössbauer spectra were collected at 10 K in a Janis SHI-850 closed-cycle refrigeration system using a WissEl spectrometer in constant acceleration mode with a ^{57}Co**Rh** source. The spectrometer was calibrated at room temperature using a 6-μm-thick α-Fe foil.

Magnetometry measurements were done using a SQUID magnetometer (Quantum Design MPMS-XL5) using dried nanoparticle samples encapsulated in a gel cap. The metal-oxide cores of the nanoparticles were separated by the protein shell. This ensured identical particle separation for all samples and prevented physical contact between the oxide cores. Hysteresis loops were collected from 2 K to 400 K after cooling the sample in an applied field of 5 T. Field-cooled and zero-field-cooled dc-susceptibility were measured using an applied field of 5 mT from base temperature to 400 K for the Fe-oxide nanoparticles and 10 K to 400 K for the cobalt-doped nanoparticles. Frequency-dependent ac-susceptibility temperature scans were measured using an oscillating field of 0.25 mT with no dc applied field. All magnetometry and susceptometry data are normalized to the total mass of the oxide component of the ferritin-based nanoparticles.

X-ray absorption spectroscopy (XAS) and x-ray magnetic circular dichroism (XMCD) measurements were done at beamline 4-ID-C at the Advanced Photon Source at Argonne National Laboratory using dried nanoparticle samples mounted on carbon tape. All spectra were recorded with a 0.1-eV resolution using the total electron yield mode, and XMCD spectra were measured by reversing the x-ray polarization at each energy interval with the XMCD and XAS spectra measured as the difference and sum, respectively, between the absorption of left- and right-circularly polarized x rays. Spectra were measured from 10 K to 200 K in applied fields from 0.25 to 5.0 T for 0% and 3% cobalt-doped samples and 0.1 T to 5.0 T for 12% cobalt-doped samples to examine the temperature and field dependence of the Fe and Co site-specific magnetism. A spectrum was collected at 50 K and 5.0 T for a 10% cobalt-doped sample to examine the Fe and Co coordination environments. All spectra were normalized to the maximum intensity at the L_3 edge of the XAS spectrum.

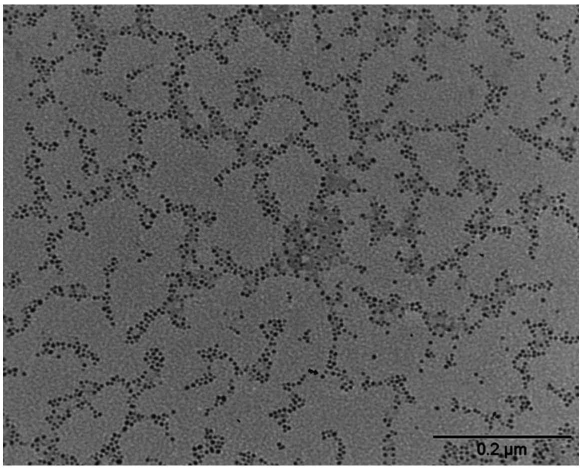

FIG. 1. A typical low-resolution TEM image of Fe-based ferritin nanoparticles.

III. RESULTS AND DISCUSSION

A. Overall structure and composition

Using the magnetic separation purification procedure to prepare the ferritin-based nanoparticles, only ferritin filled with a significant quantity of Fe_3O_4/γ-Fe_2O_3 (magnetoferritin) is retained in the column. However, we noted that only a negligible amount of unfilled nanoparticles were recovered from the flow through fractions of the column indicating that most of the protein shells were filled with metals. These results confirm that the synthetic PfFt proteins possess higher metal mineralization efficiency with respect to the human variants (see for example Ref. [2]), and this is retained also in the case of the cobalt-doped samples.

A typical transmission electron microscopy image of the undoped (0%) Fe-oxide nanoparticles is shown in Fig. 1. Size analysis reported previously for undoped Fe-oxide nanoparticles obtained using the same synthesis procedure and having the same metal loading showed highly uniform spherical particles with an average particle diameter of 6.5 ± 0.5 nm [3,4].

The XRD patterns were typical of a ~6-nm (diameter) nanoparticle with the spinel structure ($Fd\bar{3}m$) (see Fig. 2). No variation in the reflection broadening between samples was observed that indicated that the addition of cobalt did not affect the crystallinity or particle size as has been observed in some other cases using traditional solution synthesis of other ferritins [13,14]. This was consistent with the previously observed characteristics of PfFt in providing a favorable environment for the efficient formation of well-crystallized nanoparticles [10] and facilitates a comparison of the intrinsic magnetism. The lattice parameter and octahedral site occupancy varied

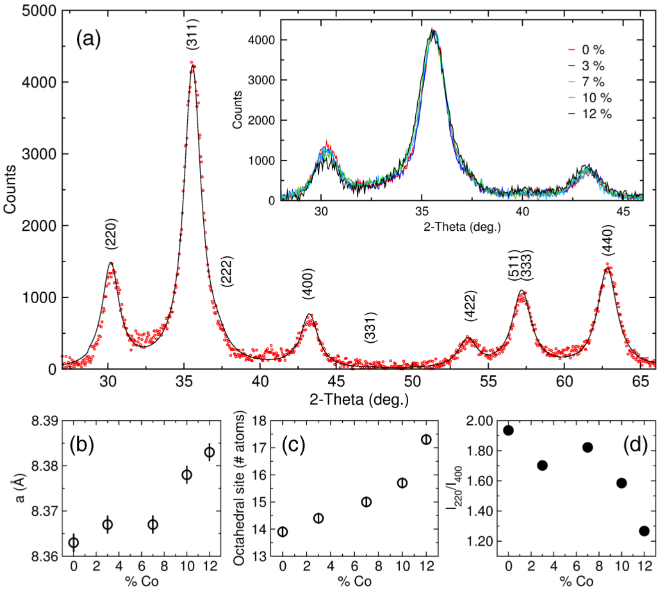

FIG. 2. (Color online) (a) X-ray diffraction pattern for undoped Fe-oxide sample, with the solid line indicating the result of the Rietveld refinement, and (inset) a selected 2θ range of the background subtracted pattern for all samples. Results of the analysis of the XRD patterns showing including (b) the lattice parameter a, (c) the octahedral site occupancy, obtained from a Rietveld refinement of the patterns, and (d) I_{220}/I_{400} variation with cobalt content.

slightly between samples, consistent with previous work which identified the composition as a mixture of γ-Fe_2O_3 and cobalt-substituted Fe_3O_4-like Fe oxides due to Co^{2+} incorporation into the octahedral sites of the spinel structure [9]. Due to significant broadening resulting from the small crystallite size and the similarity between the diffraction patterns for spinel oxides (isostructural with different lattice parameters and site occupancy only), the individual phases could not be distinguished, and one spinel component, with varying octahedral site occupancy and lattice parameter, was used for the refinement. A slight decrease in the lattice parameter was observed with increasing cobalt content, visible as a shift in the peak positions to lower 2θ. The (220) and (400) reflections are sensitive to the site occupancy of spinels [15], with the (220) reflection being sensitive to the cations in the tetrahedral site, and the (400) reflection being sensitive to cations in both the octahedral and tetrahedral sites. A change in site occupancies was indicated by a decrease in I_{220}/I_{400} with cobalt content that is consistent with an increasing octahedral site occupancy due to Co^{2+} incorporation into the structure. The octahedral site occupancy obtained from the refinements increased with cobalt content, consistent with the observed I_{220}/I_{400} change. However, the occupancy for the 12% cobalt sample was larger than the maximum 16 atoms/unit cell, and may be due to deviations in the A site or O^{2-} occupancies, which was not incorporated into the refinement. The contributions from the individual phases could not be resolved due to the substantial broadening; however, all lattice parameters were intermediate to that expected for γ-Fe_2O_3 (13.33 B site Fe^{3+} per unit cell and $a = 8.33$ Å), $CoFe_2O_4$ (16 Fe/Co per unit cell and $a = 8.38$ Å), and Fe_3O_4 (16 Fe per unit cell and $a = 8.39$ Å). The refinements of the spinel phase accounted for all of the observed reflections and their intensities, indicating that no crystalline secondary phases such as CoO or Co_3O_4 were formed. These results indicated clearly that Co^{2+} was incorporated into the Fe-oxide core.

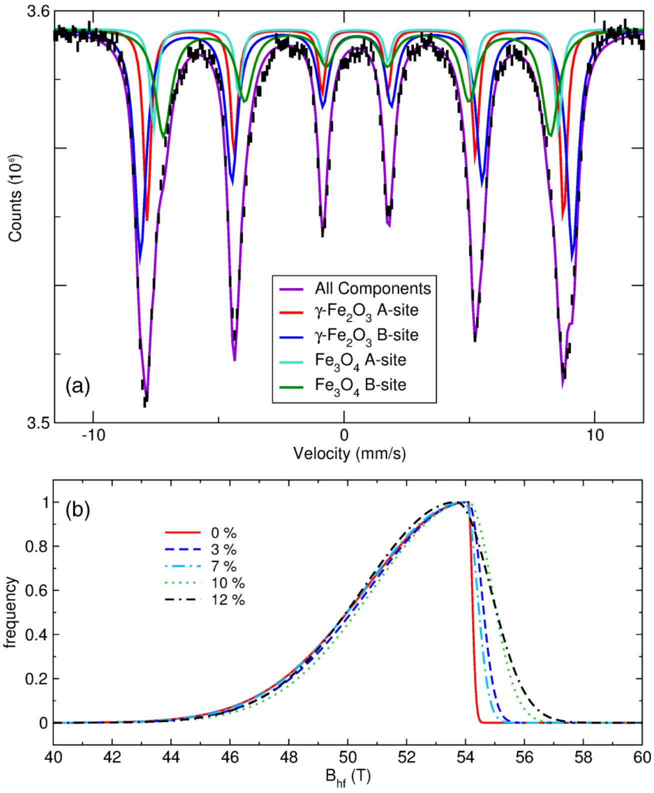

FIG. 3. (Color online) (a) Mössbauer spectrum collected at 10 K for the undoped nanoparticle sample, with the results of a component fit, described in the text, and (b) distribution of hyperfine fields (B_{hf}) observed for the Mössbauer spectra for the undoped and cobalt-doped nanoparticles that were consistent with results using individual components to represent the A and B sites of the Fe-oxide-based core [9].

We have established previously [9] the composition of the nanoparticles using Mössbauer spectra collected at 10 K which characterize the atomic ^{57}Fe electronic and magnetic environments via the hyperfine field (B_{hf}), isomer shift, and quadrupole splitting. Shown in Fig. 3(a), the spectrum for the undoped nanoparticles contained components with hyperfine parameters typical of γ-Fe_2O_3 and Fe_3O_4, with the relative weight of the spectrum components indicating a 70%/30% mix of γ-Fe_2O_3/Fe_3O_4. With the addition of Co^{2+}, a secondary low-B_{hf} component, strongly reduced Fe_3O_4 B-site absorption was measured that was consistent with the formation of a substituted Fe_3O_4-like phase [13,16,17]. A deviation from the stoichiometric A/B site ratio of 1:2 for the Fe_3O_4 component was observed that could not be accounted for by Co^{2+} substitution alone, suggesting that a B-site-deficient oxide resulted. The spectra also indicated that the composition of the nanoparticle became more Fe_3O_4-like with increasing cobalt content. Broadened linewidths $\Gamma = 0.2$–0.4 mm/s compared to the natural (source) $\Gamma_{nat} = 0.130 \pm 0.005$ mm/s indicates that the Fe ions experienced chemical disorder; the nanoparticle likely consisted of a solid solution of cobalt-doped nonstoichiometric Fe oxide that contains a changing mixture of Fe ions in γ-Fe_2O_3 and cobalt-substituted Fe_3O_4-like magnetic and electronic environments, with disorder arising from the effects of a distribution of Co^{2+} and vacancies among the B sites. The relative area of each component of a Mössbauer spectrum is proportional to the number of Fe ions characterized by the hyperfine parameters. Thus, the relative abundance of the γ-Fe_2O_3 and Fe_3O_4-like A and B sites was used to estimate the overall composition of the nanoparticle [9]. In addition, an estimate of the mass of the oxide core relative to the mass of the metal $m_{\mathrm{oxide}}/m_{\mathrm{metal}} = 1.45 \pm 0.07$ was obtained using the composition determined from the Mössbauer spectra, which, in turn, was used to normalize the mass of the magnetometry sample to the oxide content of the nanoparticles with known metal loadings [9].

Due to the significant overlap of the Fe-oxide components of the Mössbauer spectra, fits using a distribution of hyperfine fields were done, which provided a more transparent comparison of the spectrum features among the series. This was used to ensure that the qualitative changes in the spectrum features were accounted for properly and consistently with the component fits. Shown in Fig. 3, similar increases in the average B_{hf} with increasing cobalt content were observed using both fitting procedures that resulted primarily from a systematic increase in B_{hf} of each component [9]. Additionally, both fitting procedures indicated a narrow distribution of high B_{hf} and a broad distribution of low B_{hf}, with additional broadening observed for the cobalt-doped samples. The relatively broad B_{hf} distribution for all samples was consistent with the large Γ observed for the component fits.

B. Element-specific composition and magnetism

To characterize the Fe and Co coordination environments and site-specific magnetism, XAS and XMCD spectra were collected over the Fe (700–730 eV) and Co (770–800 eV) $L_{2,3}$ ($2p \rightarrow 3d$) edges for the 0%, 3%, 10%, and 12% cobalt-doped samples. XAS and XMCD spectra features vary with the iron and cobalt oxidation states and coordination environment and with the intensity of the characteristic features of each species varying with the relative abundance. The XAS and XMCD spectra for cobalt were consistent with Co^{2+} in an octahedral coordination environment such as the octahedral sites of a spinel Fe oxide, or CoO [13,18–20], and differed clearly from the spectrum expected for Co_3O_4 [21]. For iron, the XAS spectra can provide some compositional information from the relative intensities of the features at the L_3 edge (~705–715 eV) since the relative intensity of the two maxima (labeled X and Y in Fig. 4) in the L_3 edge vary with the A- and B-site occupancies. An $I_X/I_Y \sim 0.33$ and 0.62 have been measured for γ-Fe_2O_3, and Fe_3O_4, respectively [22]. A measured $I_X/I_Y = 0.40$–0.42 for the cobalt-doped ferritin samples indicates a mixture of the two Fe oxides, consistent with the other compositional information. The XMCD spectra are a measure of the spin-dependent x-ray absorption. Similarly to XAS, the XMCD features are characteristic of the coordination environments of the species present, however, in addition, the XMCD intensity is proportional to the magnetization of the ion indicated by a given spectrum feature and hence provides the site-specific magnetization. In γ-Fe_2O_3 and Fe_3O_4, the octahedral B-site Fe ions are coupled to each other ferromagnetically, the tetrahedral A-site Fe ions are coupled to each other ferromagnetically, and the A-B intersublattice coupling is antiferromagnetic. As a result, magnetization of the A site is opposite to that of the B site which splits the L_3 into three components (B_1, A, B_2; Fig. 4) whose intensities vary depending on the amount of octahedral Fe^{2+}, tetrahedral Fe^{3+}, and octahedral Fe^{3+}, respectively. For example, for γ-Fe_2O_3, B_2 is more intense than B_1 with $I_{B_1}/I_{B_2} = 0.4$. By contrast, for Fe_3O_4, B_2 is more intense than B_1, and $I_{B_1}/I_{B_2} = 1.38$. $I_{B1}/I_{B2} \sim 0.7$ was measured for the undoped sample, intermediate to the expected ratios for γ-Fe_2O_3, consistent with the relative amounts of γ-Fe_2O_3 and Fe_3O_4 (70%/30% ± 5%) determined with Mössbauer spectroscopy. A relatively large I_A/I_{B_2} was measured for all samples, and it was larger than would be expected for either Fe oxide, suggesting some B-site deficiency as well. In addition, the spectra indicated that the cobalt magnetization was aligned with the B sites of the Fe oxide, consistent with the Mössbauer spectroscopy results.

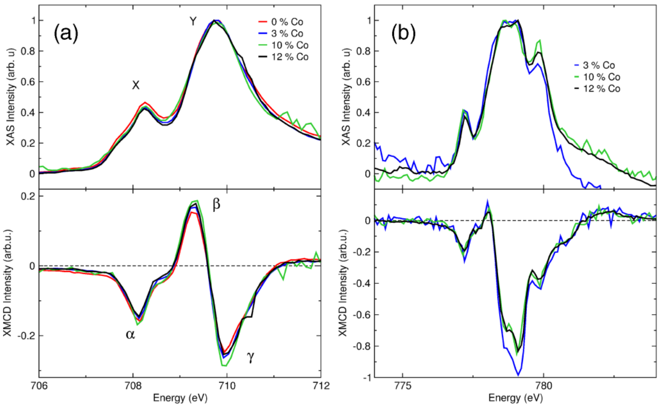

FIG. 4. (Color online) Fe (a) and Co (b) XAS (top) and XMCD (bottom) spectra for the 0% (red), 3% (blue), 10% (green), and 12% (black) cobalt-doped nanoparticles measured at 10 K and 5 T.

The Fe magnetization for each site showed only a slight temperature dependence (~5% decrease) from 10 K to 200 K that was similar for all samples (may have a slightly stronger effect on the B_2 site). A ~15% decrease in XMCD signal with increasing temperature was observed for Co in the 3% and 12% samples. This behavior was consistent with the temperature dependence of the saturation magnetization measured by magnetometry, where an ~8% decrease in M_S was measured for all samples (described below). The field-dependent elemental magnetization varied markedly between samples. Shown in Fig. 5, no change in Fe XMCD signal was measured for the undoped sample, and the field dependence became more pronounced with Co content. A larger variation in the B-site and Co^{2+} magnetizations was observed compared to the Fe A-site magnetization. A comparison with the first quarter of the hysteresis loop measurements (from +5 to 0 T Fig. 6) indicated that the Fe and Co magnetization had the same qualitative field dependence as the total magnetization.

The ratio of the orbital and spin moments for Fe and Co were determined using the sum-rule analysis [23] that results in

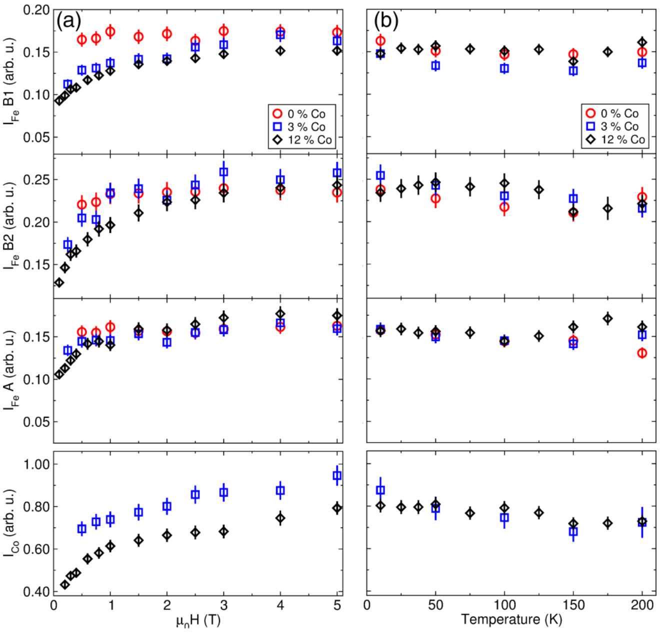

FIG. 5. (Color online) Fe and Co magnetization measured from the XMCD spectra for 0% (black circles), 3% (red squares), and 12% (blue diamonds) as a function of field (a) and temperature (b). Note that the same scale was used for all Fe sites, and the Co scales are 4× the Fe scale.

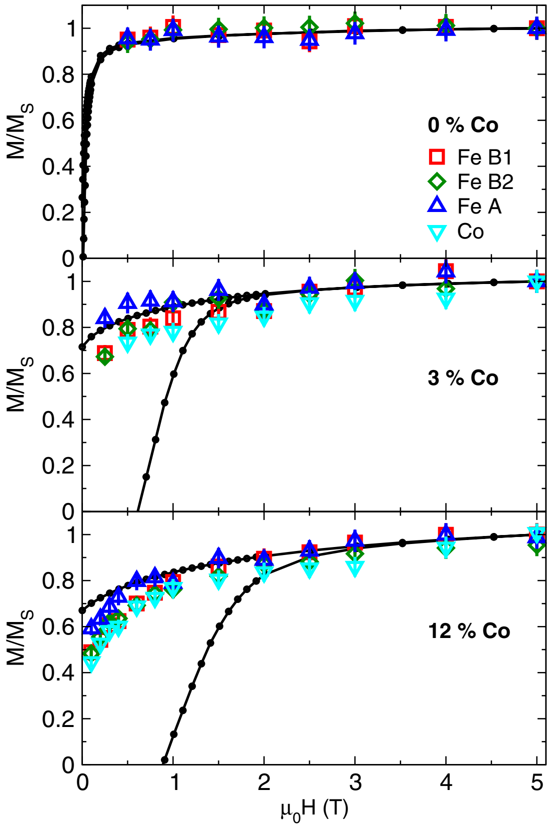

FIG. 6. (Color online) Field-dependent XMCD signal measured at 10 K for the Co (cyan ▽) and Fe B_1 (red □), B_2 (green ◇), and A sites (blue △) are shown, normalized to the value at 5 T. The first quarter of the hysteresis loops measured at 10 K are also shown (black curves).

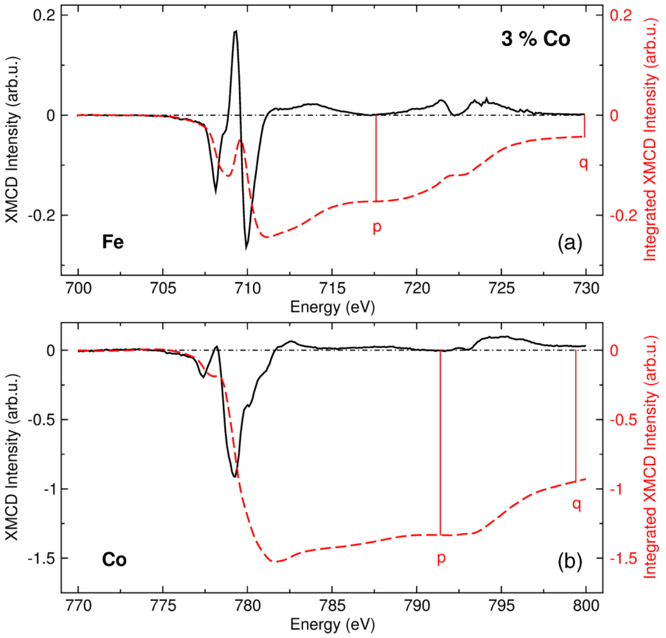

FIG. 7. (Color online) Representative XMCD spectra collected over the $L_{2,3}$ edges of Fe (a) and Co (b). The dashed lines indicate the integrated XMCD signal, and p and q were used to determine m_l/m_s using sum-rule analysis.

$m_{\mathrm{orb}}/m_{\mathrm{spin}} = 2q/(9p - 6q)$, where p and q are the integrated XMCD intensities over the L_3 edge and the combined L_3 and L_2 edges, respectively (see Fig. 7). A slow increase in integrated XMCD intensity due to an offset from zero in the XMCD signal at the highest energies was observed for all Co spectra. This was observed for spectra that were collected by reversing the incident photon helicity and by reversing the polarity of the applied field, indicating that the effect was not due to an artifact of the experimental conditions. Since the d orbitals are very localized and should not contribute significantly to the XMCD spectrum past the L_2 edge, the persisting XMCD intensity may be due to the excitation of polarized, delocalized s electrons [24,25]. Since s states are not relevant to the calculation of m_l/m_s, the integral was terminated at the point where there was no longer a slope in the XMCD intensity (799 eV). For this reason, and since it known that there are limitations to the validity of the sum rules for transition metal oxides, for example, due to mixing of the L_2 and L_3 edges that can result in a large discrepancy in the derived magnetic moments [26], we compare only the relative change in m_l/m_s between samples, having applied the same integration procedure to all spectra. No significant deviation from the expected $m_l/m_s = 0$ for spinel oxides was observed for all of the Fe spectra for all samples. The Co spectra indicated a larger orbital moment for the 12% compared to the 3% cobalt-doped nanoparticles, with the difference that persisted for various temperature and field measurements, shown in Fig. 8. The m_l/m_s values were consistent with cobalt ferrites, where crystal field effects result in an unquenched orbital moment of octahedral Co^{2+} ions [27]. The larger m_l/m_s for the sample with higher Co^{2+} suggested a more effective d-orbital overlap that was likely due to the more filled structure of the higher cobalt content samples, and a consistent

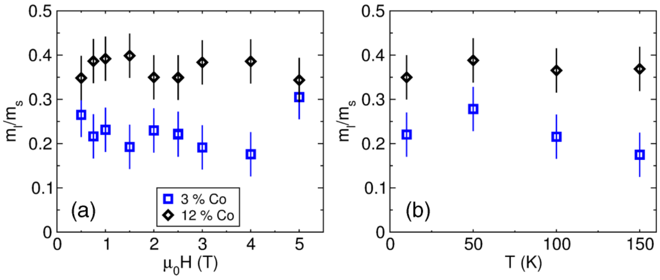

FIG. 8. (Color online) Ratio of the orbital and spin moments for Co^{2+} in the 3% and 12% cobalt-doped nanoparticles, determined using sum-rule analysis, as a function of (a) applied field and (b) temperature.

shift towards a cobalt-substituted Fe_3O_4-like composition (in comparison with the B-site-deficient γ-Fe_2O_3) with increasing cobalt content that was indicated by XRD and Mössbauer spectroscopy. In addition, while the increase in m_l/m_s could be attributed to a reduced average Fe m_s due to a (slightly) larger fraction of Fe^{2+} (vs Fe^{3+}) with increasing Co content, the increase of m_l/m_s and B_{hf} (that is affected directly by m_l) from comprehensive fits to the Mössbauer spectra using the correct site assignments [9] is more in keeping with an increasing overall Fe m_l.

C. Susceptometry (dynamics)

To examine the dynamics of the magnetism of the nanoparticle samples, ac-susceptibility measurements (Fig. 9) were done, which show clearly the difference in anisotropy and resulting superparamagnetic blocking temperature for different dopant amounts. The in-phase ac-susceptibility [$\chi'(T)$] show a frequency-dependent maximum that is characteristic of the dynamical freezing behavior of superparamagnetic nanoparticles. At the lowest temperatures the magnetization responds only weakly to the ac drive field, since the anisotropy is large compared to the thermal energy of the system. At higher temperatures the magnetization responds strongly to the ac drive field and a maximum response is obtained at the superparamagnetic blocking temperature, T_B, above which the system has sufficient thermal energy to undergo 180° spin flips within the time frame of the measurement. Above T_B, a frequency dependence is no longer observed since the nanoparticles magnetization behaves as a free paramagnetic "superspin" which exhibits no hysteresis. The out-of-phase [$\chi''(T)$] ac-susceptibility show single maxima and a strong frequency dependence near T_B, indicating maximum energy dissipation when the ac drive field is comparable to the time scale of magnetization reversal below T_B due to hysteretic processes. A shift of the maxima of $\chi'(T)$ and $\chi''(T)$ towards higher temperatures indicated clearly an increase in the superparamagnetic blocking temperature with the addition of Co^{2+}. However, it should be noted that the temperature at which the maximum was observed (which reflects the T_B for the sample) was a maximum for the 7% and 10% cobalt samples and slightly lower for the 12% sample [shown clearly in Figs. 10(a) and 12], indicating that the anisotropy determined from the fits was not simply proportional to the cobalt content of the Fe-oxide phase.

For single noninteracting uniaxial particles the frequency dependence of the maximum of $\chi'(T)$ (T_B) may be described by the Néel-Arrhenius relaxation model $\nu = \nu_0 \exp(-KV/k_B T_B)$, where ν_0 is the attempt frequency for nanoparticle magnetization rotation, ν is the measurement frequency, K is the anisotropy constant, V is the nanoparticle volume, and T_B is the temperature at which a maximum is observed in $\chi'(T)$. Fits to the frequency dependence of $T_B(\nu)$ using the Néel-Arrhenius model resulted in unphysically large $\tau_0 = 1/\nu_0$ of 10^{-15} s for the undoped and 10^{-23} s for the cobalt-doped samples, indicating interparticle interactions [28]. To obtain a physically reasonable τ_0 and to account for the effects of interactions on the energy barrier of the magnetization dynamics, the Néel-Arrhenius law is modified by $T_B \rightarrow T_B - T_0$ to obtain a Vogel-Fulcher law [28,29] $\nu = \nu_0 \exp[-KV/k_B(T_B - T_0)]$, where T_0 accounts for the effect of interparticle interactions. Shown in Fig. 10, fits using the Vogel-Fulcher law using $\tau_0 = 10^{-10}$ s indicated an increase in K from $6.33 \pm 0.05 \times 10^4$ J/m^3 for the undoped sample, to 1.4–1.5 $\times 10^5$ J/m^3 for the cobalt-doped samples. These results show that K did not differ significantly with the cobalt content of the nanoparticle, indicating that the observed change in K with the addition of cobalt was not due to single-ion effects of the highly anisotropic octahedral Co^{2+} dopant ions

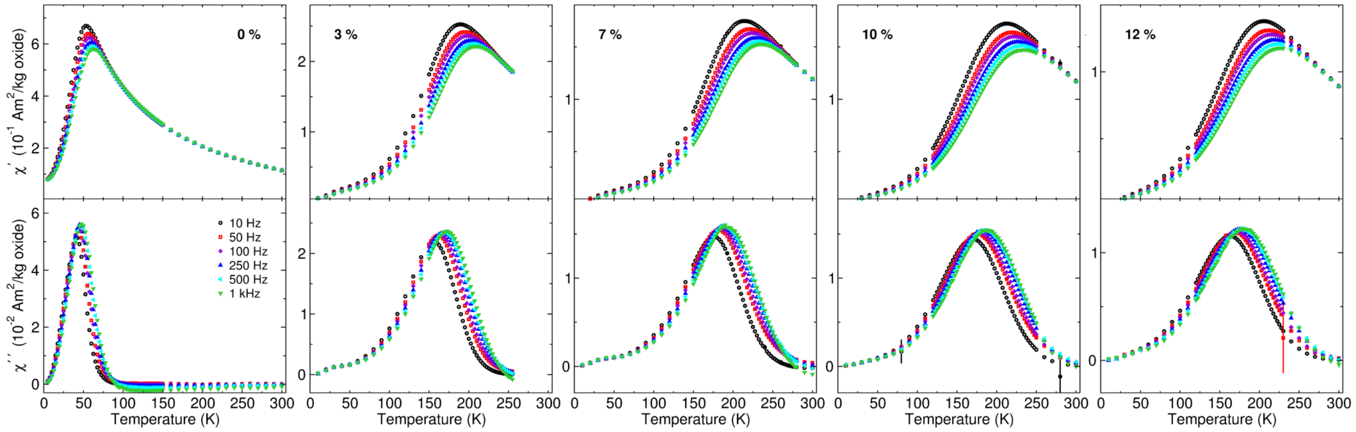

FIG. 9. (Color online) In-phase (χ') (top) and out-of-phase (χ'') (bottom) ac-susceptibility for undoped and cobalt-doped nanoparticles. Note the change in scale between samples.

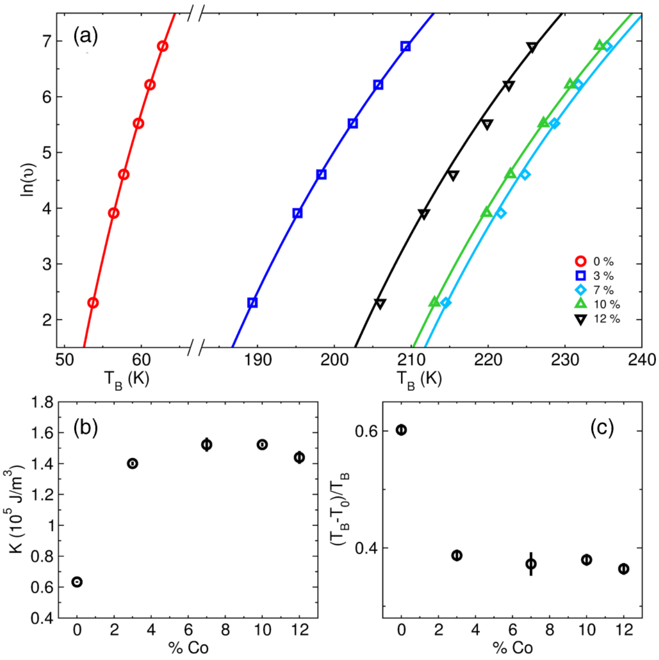

FIG. 10. (Color online) (a) Frequency dependence of the maximum of the in-phase ac-susceptibility curves, with the lines indicating a fit to the Vogel-Fulcher law. Note the break in the scale between the 0% and cobalt-doped curves. (b) The effective anisotropies and (c) values of T_0, obtained from the Vogel-Fulcher fits, relative to the temperature of the maximum of $\chi'(T)$ for 10 Hz.

alone. T_0 can be considered to describe the temperature regime where interactions are effective and above which thermal energy is sufficient for the interactions to be overcome under the conditions of the ac-susceptibility measurement. A comparison of the interaction effects was obtained by comparing T_0 relative to T_B to account for the differences in energy scales between the samples, i.e., by comparing $(T_B - T_0)/T_B$. When T_B was taken to be the temperature at which $\chi'(T)$ was a maximum for $\nu = 10$ Hz, $(T_B - T_0)/T_B$ [Fig. 11(c)] was lower for the cobalt-doped nanoparticles than for the undoped nanoparticles, indicating that interactions were more effective between the cobalt-doped nanoparticles than the undoped particles [$(T_B - T_0)/T_B = 1$ for noninteracting particles] and that interactions had a comparable effect for all cobalt dopant amounts. These results were also consistent with the expected $(T_B - T_0)/T_B$ for interacting nanoparticles [30]. The lower relative value of T_0 for the cobalt-doped samples suggested that the correlation length of the spatial fluctuations of the magnetization among the cobalt-doped nanoparticle systems [29] ($r_c \propto [(T - T_0)/T_0]^{-1/2}$) was larger in comparison to the undoped systems so that the dynamics of cobalt-doped systems involved the activation of a larger effective volume of correlated nanoparticle magnetizations.

ZFC and FC dc-susceptibility temperature dependencies were consistent with the T_B indicated by ac-susceptibility measurements and are shown in Fig. 11(a). The maximum of the ZFC curve (T_{max}) increased from 40 K for the undoped sample to 180 K for the cobalt-doped samples. Above T_{max}, an irreversibility [shown in Fig. 11(b)] that was consistent with a broadened energy barrier distribution due to interparticle interactions. Figure 12 presents $M_{\text{ZFC}}(T)$ and $\chi'(T)$ measured with a 10-Hz drive frequency which shows that both measurements indicated a slightly lower T_B for the 12% cobalt-doped sample, compared to the 7% and 10% and an overall broadening of the response curves with increasing cobalt content. Since the overall effect of interactions is to increase the energy barrier to magnetization reversal, the T_B in the presence of interactions provides an overestimate relative to the intrinsic behavior of the isolated nanoparticle. The effect of interparticle interactions was also reflected in the static

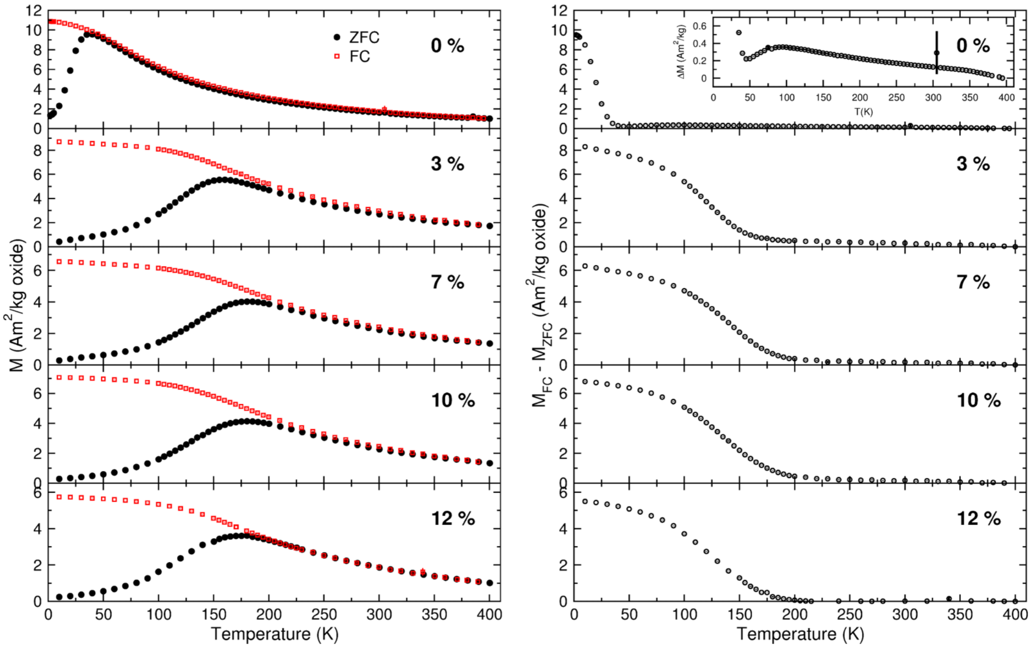

FIG. 11. (Color online) Zero-field-cooled (ZFC) (red □) and field-cooled (FC) (black ○) dc-susceptibility (right) and difference between the FC and ZFC magnetizations (right). The inset shows irreversibility persisting to high temperatures for the undoped nanoparticles.

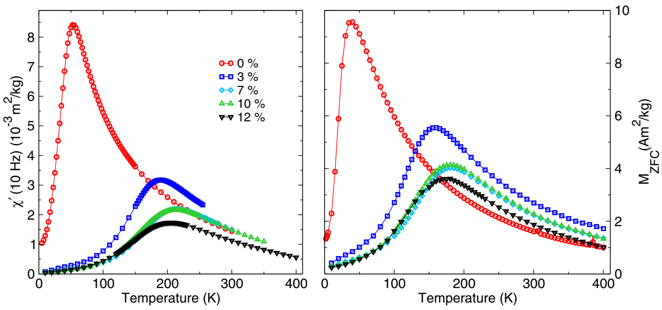

FIG. 12. (Color online) (a) In-phase (χ') ac-susceptibility curves measured using 10 Hz. (b) Zero-field-cooled magnetization curves.

susceptibility measured in low applied fields. By comparison with the ac susceptibility, where the use of an ac drive field probes the dynamical response of the interacting system, the application of a dc applied field enhances the interactions by aligning partially the magnetization of the nanoparticles. For interacting systems, a Curie-Weiss-like behavior at the highest temperatures [29] is observed, $\chi_{\mathrm{dc}}(T) = M_{\mathrm{ZFC}}(T)/\mu_0 H = \mu/(T - T_{0,\mathrm{dc}})$, where $\mu = M_S \pi D^3/6$ is the magnetization of a nanoparticle of diameter D. Shown in Fig. 13, fits to $1/\chi_{\mathrm{dc}}$ curves at high temperatures, where irreversibility effects were minimal, provided comparable $T_{0,\mathrm{dc}}$ for all samples which indicated a similar interaction field strength for all samples due to a similar magnetization, packing fraction, and particle separation enabled by the ferritin shells.

D. Magnetometry (statics)

To examine the static magnetic properties of the nanoparticles, hysteresis loop measurements were done from 2 K to 400 K. As was observed for the magnetization dynamics, the static measurements also indicated a substantial change in the magnetism of the nanoparticles that occurred with cobalt doping: large enhancements of the coercivity ($\mu_0 H_C$), anisotropy (K), and superparamagnetic blocking temperature (T_B) that varied nonsystematically with the cobalt content. No exchange bias ($\mu_0 H_{EX}$) was measured for any sample, indicating that no crystalline CoO shell was present, which was consistent with the results from XRD analysis and in contrast with other ferritin-based Co/Fe-oxide nanoparticles where segregated Co-oxide and Fe-oxide phases resulted in a significant $\mu_0 H_{EX}$ [31].

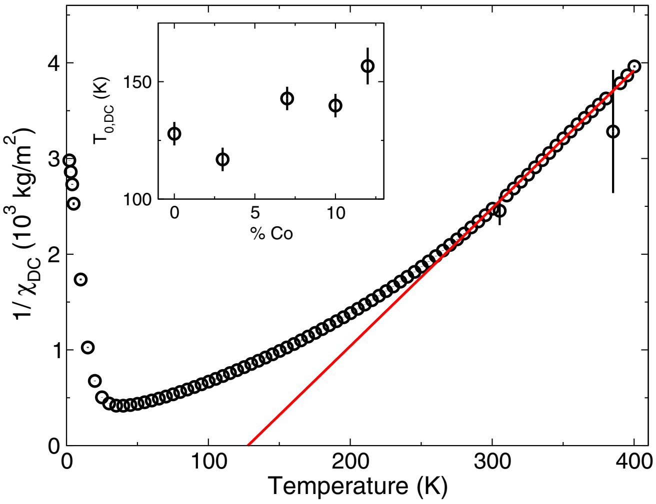

FIG. 13. (Color online) Inverse dc-susceptibility for the undoped nanoparticles, with the line indicating a fit to a Curie-Weiss-like temperature dependence. The inset shows the temperature intercept θ that reflects the effects of interparticle interactions.

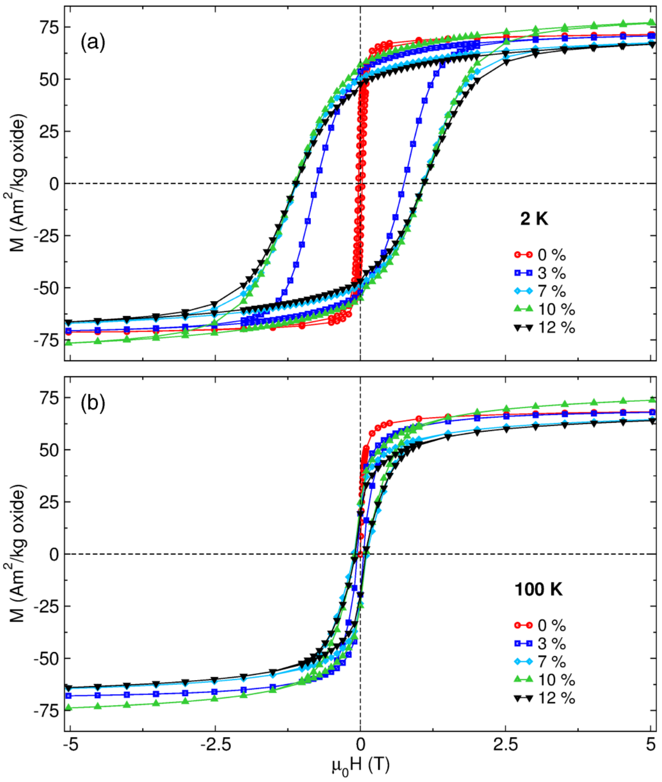

FIG. 14. (Color online) Hysteresis loops at (a) 2 K and (b) 100 K measured after cooling the samples in an applied field of 5 T.

Hysteresis loops measured after cooling the sample in a 5-T field are shown in Fig. 14. A substantial increase in coercivity with cobalt doping that did not scale with the change in T_B indicated that the change in coercivity between samples was not due to the difference in superparamagnetic relaxation behavior alone, but arose from the increase in nanoparticle anisotropy. For a uniaxial noninteracting nanoparticle, the coercivity can be related to the anisotropy by $\mu_0 H_C = 2K/M_S[1 - (T/T_B)^{1/2}]$. While interaction effects have been identified clearly from the ac-susceptibility measurements, this relationship provided a good fit to $H_C(T)$ up to $\sim T_{B,Hc}/2$ (the onset temperature of H_C), providing an estimate of K, that was nearly identical to those obtained from the Vogel-Fulcher fits from ac-susceptibility measurements and indicates the same trend in K with cobalt content (see Fig. 15). Both methods indicated that K for the cobalt-doped samples was much higher than the undoped nanoparticles, that K was not proportional to the cobalt content, and that K was a maximum for 10% cobalt doping. No improvement to the fit or significant change in the resulting K was achieved by using a $T^{2/3}$ dependence that would indicate a cubic anisotropy.

The high-field region of the hysteresis loops, showed clearly a linear positive field dependence of the magnetization at high applied fields for all samples. This high-field susceptibility

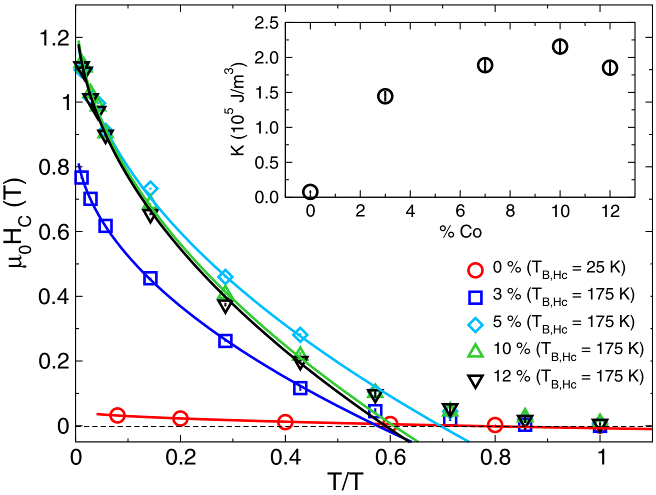

FIG. 15. (Color online) Temperature dependence of the coercivity (H_C) with the temperature rescaled to the onset temperature of the coercivity T_{B,H_c}. The lines are fits described in the text that indicate a $T^{1/2}$ dependence. The inset shows the anisotropy constant (K) determined from the temperature dependence of H_C.

(χ_{HF}) was significantly larger for the cobalt-doped samples than the undoped Fe-oxide nanoparticles and displayed a temperature dependence. For a typical nanophase ferromagnet or ferrimagnet, the magnetization curves for $T > T_B$ should follow a Langevin behavior so that $M_{\mathrm{LAN}}(x) = M_S L(x)$ or, if modified to include a term for a high-field (linear) susceptibility, $M_{\mathrm{LAN}}(x) = M_S L(x) + \chi_{\mathrm{HF}} H$, where M_S is the saturation magnetization, χ_{HF} is the linear high-field susceptibility, and $L(x) = \coth(x) - 1/x$ is the Langevin function, where $x = \mu(T)H/k_B T$ and $\mu(T)$ is the magnetic moment of each nanoparticle core. However, as shown in Fig. 16, the magnetization curves for $T > T_B$ do not lie on a common M vs H/T or $(M - \chi_{\mathrm{HF}} H)$ vs H/T curve, indicating a deviation form typical Langevin behavior (not a simple superparamagnet) that could be a result of a high surface anisotropy that prevents free rotation of the magnetization (as assumed by the Langevin model).

The temperature dependence of the high-field susceptibility is shown in Fig. 17. The temperature dependence of χ_{HF} indicated a paramagneticlike behavior for $T < 250$ K, following a Curie-Weiss dependence $\chi(T) = C/(T - \theta)$ (shown in Fig. 18), where C is the Curie constant $C = N\mu_B^2 p_{\mathrm{eff}}^2/3k_B$ that provides the effective moment p_{eff} and θ describes the interactions among the ions contributing to χ_{HF}. This indicated that there are clusters of ions within the ferritin shell that behave like paramagnets. Since this behavior was not observed in the un-doped nanoparticles, this indicated that the origin of the effect was the Co^{2+} ions, such as Co^{2+}-based clusters. The elemental data (XAS, XMCD, and Mössbauer spectroscopy) for cobalt indicated only octahedrally coordinated Co^{2+}, consistent with Co^{2+} dopant ions in the B sites of Fe oxide or with CoO. This Curie-Weiss analysis also provided negative $\theta \sim -(70\text{–}100)$ K that is consistent with antiferromagnetic interactions and strongly reduced exchange due to the small cluster size ($T_{N,\mathrm{CoO}} = 290$ K).

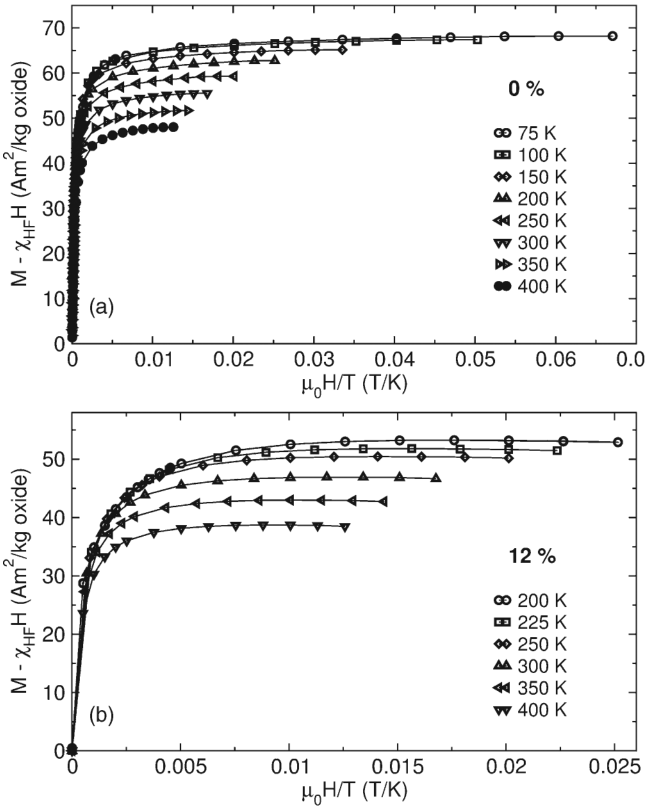

FIG. 16. $(M - \chi_{\mathrm{HF}} H)$ vs H/T curves measured for $T > T_B$ for (a) undoped and (b) 12% cobalt-doped nanoparticles.

Using this analysis, a CoO cluster size of $\leqslant\sim 0.7$ nm could reasonably fit within the ferritin cavity (in addition to the Fe-oxide core), but may not contribute noticeably to the XRD pattern and would not provide a measurable H_{EX}, especially if the cluster was not well crystallized. A reasonable cluster p_{eff} of $\sim$50–60 was obtained assuming maximum cluster diameter of 0.7 nm and a minimum of 50% of the available Co^{2+}-forming clusters rather than substituting into the Fe-oxide-based core. For larger fractions of the

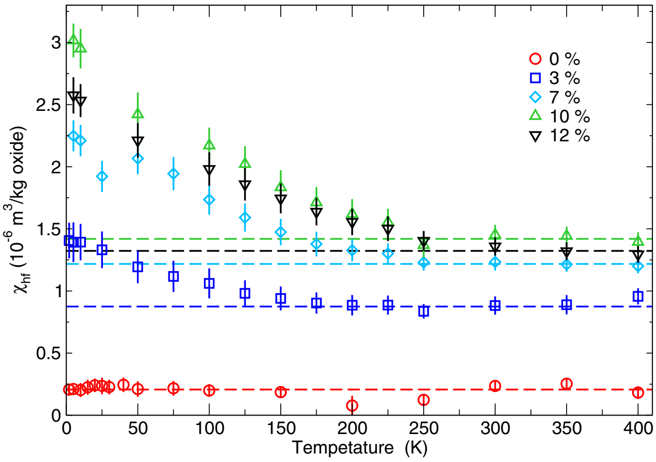

FIG. 17. (Color online) Temperature dependence of the high-field susceptibility $\chi_{\mathrm{HF}}(T)$. The dashed lines indicate the contribution due to a surface anisotropy, which is independent of temperature.

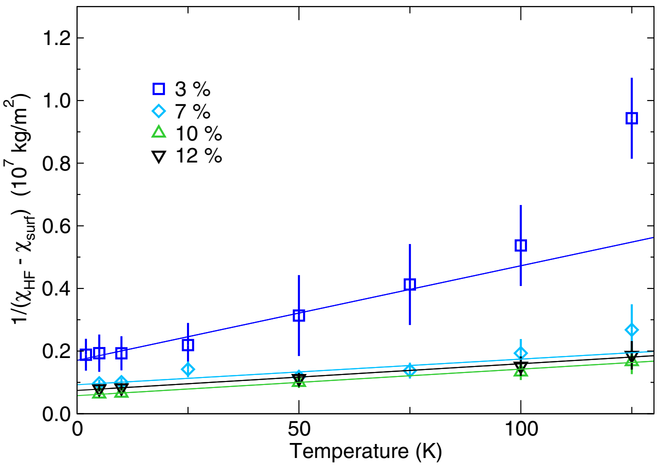

FIG. 18. (Color online) Temperature dependence of the inverse high-field susceptibility $\chi_{HF}(T)$, where the constant offset due to the surface anisotropy [$\chi_{surf}(T)$] has been subtracted.

available Co^{2+}-forming clusters, a lower p_{eff} was obtained, although more clusters are required; however, a range of Co^{2+} fractions from 50% to 100% provided a reasonable p_{eff} of $\sim$4.7–6.5/Co^{2+} (50%) and $\sim$3.8 for 100%, while providing a reasonable overall fraction of the volume to the clusters (i.e., the clusters would easily fit within the ferritin shell, in addition to the Fe-oxide-based core that takes up the largest fraction of the total volume). However, since the Mössbauer spectroscopy and the magnetometry showed clearly the effect of Co^{2+} incorporation into the Fe-oxide core, the limit of 100% Co incorporation into the clusters is not possible. While we cannot yet provide a definite degree of cobalt incorporation into the Fe oxide, a cobalt distribution of 50% clusters, 50% dopant ions in the oxide provides reasonable results that are consistent with all of the other data (elemental, atomic, and magnetometry) that we have available. This cluster description accounts for the measured χ_{HF} for $T < 250$ K for the cobalt-doped nanoparticles. In addition, the likelihood of these CoO clusters residing outside the PfFt synthetic ferritin shell is remote at best; any impurities and metal-ion or cluster aggregates left on the ferritin exterior after sample preparation and purification would defeat the unique, macroscopic crystallization of three-dimensional nanoparticle assemblies [1,4] made using these nanoparticle building blocks.

The temperature-independent behavior of χ_{HF} that was observed for the un-doped nanoparticles and for $T > 250$ K in the cobalt-doped nanoparticles (above the ordering temperature of the CoO clusters) was consistent with a surface anisotropy. In nanoparticles, a surface anisotropy results from broken exchange bonds at the surface of the particle [32,33] and has a magnitude that depends on the sign and strength of the exchange interactions between the ions that is determined by structure, the ionic species, and their coordination environment, the result of which is a temperature-independent χ_{HF}. The Langevin description (that results in an H/T scaling of the magnetization curves) does not account for anisotropy and hence the existence of a surface anisotropy accounts for the lack of scaling observed for the nanoparticle samples.

There have been other factors discussed in the literature that can produce a positive χ_{HF}. For example, χ_{HF} has been shown to result from a significant distribution of particle sizes [34]. For a large particle-size distribution, the magnetization should remain a function of H/T, and magnetization curves measured above the superparamagnetic blocking temperature should scale accordingly, which is not observed for the samples discussed herein (shown in Fig. 16). In addition, the particle-size information from TEM and the results from the low-field dc and ac-susceptibility measurements and from the metal loading factor measurements are inconsistent with a large distribution of particle sizes.

It should also be noted that these alternate descriptions are for single-phase nanoparticles and not for mixtures of more than one magnetic phase, as exists in the cobalt-doped ferritin-based nanoparticles. When multiple phases are present, the analysis becomes significantly more complex. If there are multiple-sized particles within the system (as would occur with the cluster scenario presented), the low-field behavior is dominated by the largest particles, while the high-field behavior is dominated by the smallest particles (i.e., a careful comparison of the low-field susceptibilities, such as the ac- and dc-susceptibility measurements, and the hysteresis loop measurements must be made). The examples that exist in the literature that describe mixed-phase systems provide a more limited physical discussion (e.g., a simple combination of two Langevin functions) than exists for the single-phased systems (described above) and also do not show similar behavior to that observed in the cobalt-doped ferritin nanoparticles [35,36].

Following a subtraction of χ_{HF}, the saturation magnetization [$M_S(T)$] was obtained using the empirical law of approach to saturation $M_H = M_S(T)(1 - a/H - b/H^2)$, where M_H is the component of the magnetization in the applied field direction, M_S is the saturation magnetization, and a, b, and c are phenomenological constants (see Fig. 19). At 5 K, M_S was 73 ± 3 emu/g oxide for the undoped nanoparticles, which is in agreement with previous measurements [10], and 69 ± 2, 63 ± 2, 71 ± 3, and 60 ± 2 emu/g for the 3%, 7%, 10%, and 12% doped nanoparticles, respectively, after a correction for the ferritin masses. Since the total magnetization of the (ferrimagnetic) spinel is a result of an imbalance of the A-site and B-site magnetizations (with more B sites than A sites resulting in a nonzero magnetization for γ-Fe_2O_3, for example), a less B-site-deficient structure may account for the relatively high M_S value of the 10% sample compared to the other cobalt-doped nanoparticles, a feature that was consistent with the results from Mössbauer spectroscopy. The near bulk values of M_S, compared with bulk γ-Fe_2O_3 $M_S = 74$ emu/g, Fe_3O_4 $M_S = 84$ emu/g, and $CoFe_2O_4$ $M_S = 80$ emu/g, measured here were surprisingly large for a nanoscale materials (where a substantial reduction in M_S is often the result of intrinsic and surface disorder or poor crystallinity) and were consistent with a well-crystallized oxide core indicated by our results and previous work using the PfFt ferritin [10]. The relatively high M_S values indicate that most, if not all, of the available moments were incorporated into the particles' M_S: No indication of a disordered surface spin population which would produce an exponential-like decrease in $M_S(T)$ with increasing temperature, disorder effects in the Mössbauer spectra, or pinned magnetization measured by XMCD [37] was

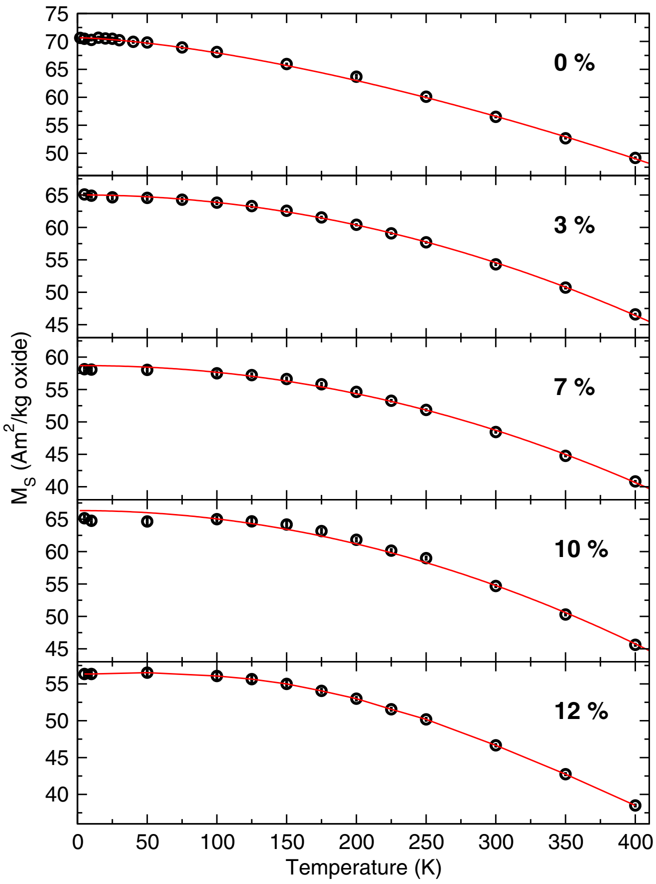

FIG. 19. (Color online) Temperature dependence of the saturation magnetization [$M_S(T)$]. The lines indicate a fit described in the text.

observed. A similar, nonsystematic variation of M_S and K with increasing cobalt substitution has been reported elsewhere (for example, Refs. [14,38]); however, systematic variations in M_S and K [13] and variation in K with no change in M_S [39] have also been reported. The wide variability of the reported overall effects of cobalt incorporation further emphasizes the need for a complete determination of the details of the structure and composition to assess properly the nature of the magnetism, since the degree of inversion, crystallinity, surface properties, and particle size will all contribute to variations in M_S and K.

The temperature dependence of M_S is due to spin-wave excitations. In the bulk, $M_S(T)$ is described by the Bloch $T^{3/2}$ law, $M_S(T) = M_0(1 - BT^{\alpha})$, where α is equal to 3/2 and B is the Bloch constant ($\propto 1/J$). For the undoped particles, $M_S(T)$ was well represented by the normal Bloch law ($\alpha = 3/2$) and provided $B = 3.83(3) \times 10^{-5}$ $\mathrm{K}^{-3/2}$, consistent with an Fe-oxide nanoparticle [40,41]. Modifications to the Bloch law are obtained when a gap in the spin-wave spectrum results from a high crystalline anisotropy [42] or due to finite-size effects [43,44]. In such systems, $M_S(T)$ appears to follow an effective power law $M_S(T) = M_0(1 - B_{\mathrm{eff}}T^{\alpha})$ where $\alpha = 1.5$–2 [44,45]. For the cobalt-doped samples a $B_{\mathrm{eff}} \sim 2 \times 10^{-6}$ K^{-2} was determined, consistent with a cobalt-ferrite-like composition [46]. In addition, $\alpha = 2$ was required to describe $M_S(T)$, which may reflect a higher intrinsic anisotropy, since the particle sizes of the doped and undoped samples were not significantly different. The difference in $M_S(T)$ behavior between the undoped and cobalt-doped nanoparticles was also consistent with the dynamical behavior of the nanoparticles that indicated clearly a difference in the effects of interparticle interactions. A change in the correlation between the magnetization of the nanoparticles that was indicated by the susceptibility measurements is consistent with a change in spin-wave behavior, since both reflect a change in the effectiveness of the dipolar coupling between particles. That is, the change from $\alpha = 3/2$ to $\alpha = 2$ may also be the result of the significantly longer correlations of the magnetization between nanoparticles for the cobalt-doped samples that was indicated by the ac-susceptibility measurements, in addition to the higher intrinsic anisotropy, since both factors affect the establishment of spin-wave excitations within the system

IV. SUMMARY

The structure and magnetism of cobalt-doped iron-oxide nanoparticles prepared using the synthetic ferritin PfFt has been described. By examining in detail the structure using XRD, Mössbauer spectroscopy, and polarized x-ray techniques, we have established that cobalt incorporates into the octahedral B sites of the iron-oxide nanoparticles, which modifies substantially the intrinsic anisotropy due to single-ion effects of Co^{2+}. In addition, a change in the orbital moment of the Co^{2+} ions with increasing cobalt content was observed. We show that no crystalline secondary cobalt-oxide phase formed, but that a substantially enhanced surface anisotropy occurs with the addition of cobalt, and a paramagneticlike contribution to the high-field susceptibility results from cobalt ions at the nanoparticle surface. In addition to enabling a characterization of the changes in the intrinsic magnetism occurring with cobalt doping due to a consistent particle loading (size) and crystallinity, the fixed interparticle spacing provided by the PfFt shell allows a comparison of the interparticle interactions, revealing substantially enhanced correlations with the addition of cobalt.

ACKNOWLEDGMENTS

The authors thank the Natural Sciences and Engineering Research Council of and the Canada Foundation for Innovation. Use of the Advanced Photon Source, an Office of Science User Facility operated for the U.S. Department of Energy (DOE) Office of Science by Argonne National Laboratory, was supported by the U.S. DOE under Contract No. DE-AC02-06CH11357.

---

[1] O. Kasyutich, A. Illari, A. Fiorillo, D. Tatchev, A. Hoell, and P. Ceci, J. Am. Chem. Soc. **132**, 3621 (2010).

[2] M. J. Parker, M. A. Allen, B. Ramsay, M. T. Klem, M. Young, and T. Douglas, Chem. Mater. **20**, 1541 (2008).

[3] R. D. Desautels, O. Kasyutich, and J. van Lierop, J. Appl. Phys. **107**, 09B512 (2010).

[4] M. A. Kostiainen, P. Ceci, M. Fornara, P. Hiekkataipale, O. Kasyutich, R. J. M. Nolte, J. L. M. Cornelissen, R. D. Desautels, and J. van Lierop, ACS Nano **5**, 6394 (2011).

[5] M. A. Kostiainen, P. Hiekkataipale, A. Laiho, V. Lemieux, J. Seitsonen, J. Ruokolainen, and P. Ceci, Nat. Nanotechnol. **8**, 52 (2013).

[6] K. K. W. Wong and S. Mann, Adv. Mater. **8**, 928 (1996).

[7] M. Uchida, S. Kang, C. Reichhardt, K. Harlen, and T. Douglas, Biochim. Biophys. Acta **1800**, 834 (2010).

[8] E. Skoropata, R. D. Desautels, O. Kasyutich, P. Ceci, A. Fiorillo, D. Tatchev, and J. van Lierop, unpublished results, 2014.

[9] E. Skoropata, P. Ceci, O. Kasyutich, and J. van Lierop, J. Appl. Phys. **111**, 07B531 (2012).

[10] M. Fittipaldi, C. Innocenti, P. Ceci, C. Sangregorio, L. Castelli, L. Sorace, and D. Gatteschi, Phys. Rev. B **83**, 104409 (2011).

[11] O. Kasyutich, A. Saura, and W. Schwarzacher, J. Phys. D: Appl. Phys. **41**, 134022 (2008).

[12] J. Rodrǵuez-Carvajal, Physica B **192**, 55 (1993).

[13] J. M. Byrne, V. C. Coker, S. Moise, P. L. Wincott, D. J. Vaughan, F. Tuna, E. Arenholz, G. van der Laan, R. A. D. Pattrick, J. R. Lloyd, and N. D. Telling, J. R. Soc., Interface **10**, 20130134 (2013).

[14] E. Fantechi, C. Innocenti, M. Zanardelli, M. Fittipaldi, E. Falvo, M. Carbo, V. Shullani, L. Di Cesare Mannelli, C. Ghelardini, A. M. Ferretti, A. Ponti, C. Sangregorio, and P. Ceci, ACS Nano **8**, 4705 (2014).

[15] H. Ohnishi and T. Teranishi, J. Phys. Soc. Jpn. **16**, 35 (1961).

[16] E. De Grave, R. M. Persoons, R. E. Vandenberghe, and P. M. A. de Bakker, Phys. Rev. B **47**, 5881 (1993).

[17] R. M. Persoons, E. De Grave, P. M. A. de Bakker, and R. E. Vandenberghe, Phys. Rev. B **47**, 5894 (1993).

[18] S. Imada and T. Jo, J. Magn. Magn. Mater. **104**, 2001 (1992).

[19] F. M. F. de Groot, M. Abbate, J. van Elp, G. A. Sawatsky, Y. J. Ma, C. T. Chen, and F. Sette, J. Phys.: Condens. Matter **5**, 2277 (1993).

[20] G. van der Laan, E. Arenholz, R. V. Chopdekar, and Y. Suzuki, Phys. Rev. B **77**, 064407 (2008).

[21] F. Morales, F. M. F. de Groot, P. Glatzel, E. Kleimenov, H. Bluhm, M. Hävecker, A. Knop-Gericke, and B. M. Weckhuysen, J. Phys. Chem. B **108**, 16201 (2004).

[22] E. Lee, D. H. Kim, J. Hwang, K. Lee, S. Yoon, B. J. Suh, K. H. Kim, J.-Y. Kim, Z. H. Zhang, B. Kim, B. I. Min, and J.-S. Kang, Appl. Phys. Lett. **102**, 133703 (2013).

[23] C. T. Chen, Y. U. Idzerda, H.-J. Lin, N. V. Smith, G. Meigs, E. Chaban, G. H. Ho, E. Pellegrin, and F. Sette, Phys. Rev. Lett. **75**, 152 (1995).

[24] K. Kuepper, M. Raekers, C. Taubitz, M. Uhlarz, C. Piamonteze, F. M. F. de Groot, E. Arenholz, V. R. Galakhov, Y. M. Mukovskii, and M. Neumann, J. Phys.: Condens. Matter **24**, 435602 (2012).

[25] W. L. O'Brein, B. P. Tonner, G. R. Harp, and S. S. P. Parkin, J. Appl. Phys. **76**, 6462 (1994).

[26] C. Piamonteze, P. Miedema, and F. M. F. de Groot, Phys. Rev. B **80**, 184410 (2009).

[27] J. C. Slonczewski, Phys. Rev. **110**, 1341 (1958).

[28] S. Shtrikman and E. P. Wolfarth, Phys. Lett. A, **85**, 467 (1981).

[29] R. W. Chantrell and E. P. Wolfarth, J. Magn. Magn. Mater. **40**, 1 (1983).

[30] J. L. Dormann, L. Bessais, and D. Fiorani, J. Phys. C: Solid State Phys. **21**, 2015 (1988).

[31] M. T. Klem, D. A. Resnick, K. Gilmore, M. Young, Y. U. Idzerda, and T. Douglas, J. Am. Chem. Soc. **129**, 197 (2007).

[32] R. H. Kodama, A. E. Berkowitz, E. J. McNiff, Jr., and S. Foner, Phys. Rev. Lett. **77**, 394 (1996).

[33] J. M. D. Coey, Phys. Rev. Lett. **27**, 1140 (1971).

[34] D. E. Madsen, S. Mørup, and M. F. Hansen, J. Magn. Magn. Mater. **305**, 95 (2006).

[35] R. J. Usselman, M. T. Klem, S. E. Russek, M. Young, T. Douglas, and R. B. Goldfarb, J. Appl. Phys. **107**, 114703 (2010).

[36] J. Curiale, M. Granada, H. E. Troiani, R. D. Sánchez, A. G. Leyva, P. Levy, and K. Samwer, Appl. Phys. Lett. **95**, 043106 (2009).

[37] E. Skoropata, R. D. Desautels, C.-C. Chi, H. Ouyang, J. W. Freeland, and J. van Lierop, Phys. Rev. B **89**, 024410 (2014).

[38] E. Fantechi, G. Campo, D. Carta, A. Corrias, C. de Julián Fernández, D. Getteschi, C. Innocenti, F. Pineider, F. Rugi, and C. Sangregorio, J. Phys. Chem. C **116**, 8261 (2012).

[39] D. Khalafalla and A. H. Morrish, J. Appl. Phys. **43**, 624 (1972).

[40] B. Martinez, A. Roig, X. Obradors, E. Molins, A. Rouanet, and C. Monty, J. Appl. Phys. **79**, 2580 (1996).

[41] G. F. Goya, T. S. Berquó, F. C. Fonseca, and M. P. Morales, J. Appl. Phys. **94**, 3520 (2003).

[42] K. Niira, Phys. Rev. **117**, 129 (1960).

[43] P. V. Hendriksen, S. Linderoth, and P.-A. Lindgård, J. Magn. Magn. Mater. **104**, 1577 (1992).

[44] P. V. Hendriksen, S. Linderoth, and P.-A. Lindgård, J. Phys.; Condens. Matter **5**, 5675 (1993).

[45] R. H. Kodama, J. Magn. Magn. Mater. **200**, 359 (1999).

[46] C. Vasquéz-Vasquéz, M. A. López-Quintela, M. C. Buján-Núñez, and J. Rivas, J. Nanopart. Res. **13**, 1663 (2011).